Research Square

Preprints are preliminary reports that have not undergone peer review.
They should not be considered conclusive, used to inform clinical practice,
or referenced by the media as validated information.

Ultra-intense laser-driven MeV bremsstrahlung generation using foams and high-Z converters

Sebastian Busch

S.Busch@iap.uni-frankfurt.de

Goethe University Frankfurt https://orcid.org/0009-0003-8200-7256

Olga N. Rosmej

Parysatis Tavana

Mikhail Gyrdymov

Jakub Cikhardt

Ekaterina Kozlova

Alessandro Tentori

Uwe Spillmann

Thomas Kühl

GSI Helmholtzzentrum für Schwerionenforschung https://orcid.org/0000-0001-6306-4579

Pascal Boller

Christian Spielmann

Friedrich Schiller University Jena https://orcid.org/0000-0002-5223-4170

Nikolay Andreev

Joachim Jacoby

Article

Keywords: Low-density foam, direct laser acceleration, high-Z converter, MeV bremsstrahlung, photo-nuclear reactions, isotopes

Posted Date: May 13th, 2026

DOI: https://doi.org/10.21203/rs.3.rs-9104336/v1

License: This work is licensed under a Creative Commons Attribution 4.0 International License.
Read Full License

Additional Declarations: There is **NO** Competing Interest.

Ultra-intense laser-driven MeV bremsstrahlung generation using foams and high-Z converters

*S. Busch[1,2,3], O. N. Rosmej[1,2,3], P. Tavana[1,3,4], M. Gyrdymov[1,3], J. Cikhardt[5], E. Kozlova[3], A. Tentori[3], U. Spillmann[3], T. Kühl[3], P. Boller[3,6], C. Spielmann[4], N. E. Andreev[7] and J. Jacoby[1]

1 Institute for Applied Physics (IAP), Goethe University Frankfurt, Frankfurt am Main, Germany
2 Helmholtz Forschungsakademie Hessen für FAIR, Darmstadt, Germany
3 GSI Helmholtzzentrum für Schwerionenforschung GmbH, Darmstadt, Germany
4 Institute of Optics and Quantum Electronics (IOQ), Friedrich Schiller University Jena, Jena, Germany
5 Faculty of Electrical Engineering, Czech Technical University in Prague, Prague, Czechia
6 Technical University of Darmstadt, Institute for Applied Physics, Darmstadt, Germany
7 Joint Institute for High Temperatures, Russian Academy of Science, Moscow, Russia

***Correspondence**: S.Busch@iap.uni-frankfurt.de

Keywords: Low-density foam, direct laser acceleration, high-Z converter, MeV bremsstrahlung, photo-nuclear reactions, isotopes

Abstract

Intense and prompt sources of hard X-rays are an important diagnostic tool in experiments on high-energy-density science, inertial confinement fusion and laboratory astrophysics driven by high-energy high-power lasers. We have successfully demonstrated the generation of ultra-intense MeV bremsstrahlung by the interaction of high-current direct laser accelerated electrons generated in pre-ionized low-density foam with a high-Z converter. The spectral and intensity properties of the bremsstrahlung in a wide photon energy range were determined by analyzing the isotope production in photo-nuclear reactions and the dose delivered by hard X-rays after passing thick filter stack. The experiments yielded collimated MeV gamma-beams with up to 10^{13} ph/sr between 0.1 and 1 MeV and up to 10^{12} ph/sr in the giant dipole resonance, which exceeds the number of photons per joule of laser energy in comparable laser systems by an average factor of ten.

1. Introduction

High-energy-density plasmas (HED plasmas) generated in inertial confinement fusion (ICF)-relevant experiments by kJ-class lasers such as e.g. the National Ignition Facility (NIF) in the USA, the Laser Mégajoule (LMJ) in France, the XG-III in China, have large areal densities, are often short-lived and far from equilibrium. Furthermore, they themselves are intense sources of radiation. To provide critical insight into various processes undergoing in HED plasmas, pulsed sources of highly penetrating photons are of great importance. Due to high level of background radiation in experiments at large scale laser facilitates, a broad band radiation with a high photon fluence (>10^{10} photons/keV/sr) in the 10 keV–1 MeV range is required [1].

For laboratory astrophysics and medical applications, laser-driven MeV X-rays with energies in the range of giant dipole resonance (GDR) [2] are used, which enable the production of isotopes and neutrons through photonuclear reactions [3–5]. Isotopes and neutrons can be used in radio-oncology [6, 7], fast neutron resonance radiography (FNRR) [8] and resonance spectroscopy [9], generation of excited isomers [10], investigation of fast neutron capture

processes in the laboratory [11, 12], etc. Photonuclear reactions can also be used to characterize the elemental composition of materials using photon activation analysis (PAA) [13].

The optimization of laser-driven particle and radiation sources is closely linked to the efficient coupling of laser energy into relativistic electrons, which in turn depends on the acceleration mechanism. In case of kJ-class, sub-ps laser pulses, a well-developed self-modulated laser wake-field acceleration (SM-LWFA) technique [14, 15] provides an efficient platform for generating broadband X-ray and MeV bremsstrahlung sources using super-sonic gas-jets [1, 16, 17].

Effective coupling of the laser energy to electrons leading to isotope production up to ^{192}Au was achieved in interaction of the NOVA [18] laser systems with solid targets. This happens due to effective acceleration of electrons in extended plasma plume caused by a nanosecond ASE at the level of 10^{-3}–10^{-4} in case described in [18, 19] or by application of a ns heating beam forerunning the relativistic laser pulse in [20]. Direct laser acceleration (DLA) of electrons in such plasmas leading to generation of high-current collimated beams of super-ponderomotive electrons is proposed and discussed in [21, 22] and updated for the case of a large focal spot characteristic for PW, kJ-class lasers in [23].

In the case of DLA, the relativistically intense laser pulse interacts with plasma of near critical electron density (NCD) and creates a plasma channel with strong radial fields. The radial inhomogeneity of the electron density due to the ponderomotive expulsion of background plasma electrons from the channel produces a radial quasi-static electrostatic field, and at the same time, the current of accelerated electrons generates an azimuthal magnetic field. When a relativistic electron becomes trapped within the channel, it begins oscillating transversely. This betatron motion allows for very efficient energy transfer from the electro-magnetic wave of the laser light to electrons, when the betatron oscillation frequency matches the Doppler-shifted frequency of the laser. [21, 22]. Direct laser acceleration, self-modulated laser wake field acceleration (SM-LWFA), stochastic heating [24] or a combination of these mechanisms can be realized, depending on the plasma density and laser intensity.

In this work, we demonstrate an ultra-intense DLA-based source of MeV bremsstrahlung by application of pre-ionized low-density polymer foam, consisting of carbon, oxygen and hydrogen (hereinafter referred to as CHO) or carbon and hydrogen (CH) and high-Z converter as a target in experiments at relativistically moderate laser intensity.

2. Results and discussion

a. Generation of DLA-electrons

In experiments at the sub-PW Nd:glass laser PHELIX [25, 26], performed at intensity of 10^{19} W/cm^2, the effective direct laser acceleration of electrons in low-density foams [27] converted into plasma by a controlled nanosecond pulse was successfully demonstrated [28–30]. The density of the NCD plasma (e.g. 10^{21} cm^{-3} for 1 μm laser wavelength) is up to two orders of magnitude higher than in gas jets, therefore a high total charge of the accelerated electrons having Maxwellian-like energy distribution is expected. Furthermore, foams pre-

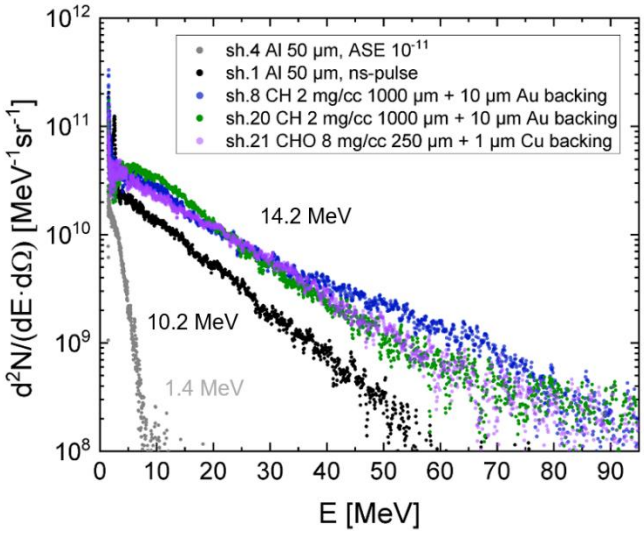
ionized by a controlled ns-pulse, allow to form plasma with a scale-length of up to hundreds of μm, thereby providing a long acceleration path for electrons under the action of a relativistically intense laser pulse. A rather weak dependence of the DLA process on the plasma profile, which has an underdense up-ramp and NCD parts, was demonstrated using 3D PIC simulations and confirmed in experiments [30].

The application of pre-ionized, low-density polymer foams as targets results in high-current directed beams of electrons with effective temperatures 10–15 times higher than the ponderomotive potential of 1.5 MeV and electron energies up to 100 MeV and higher. The DLA electrons with energies exceeding 7.5 MeV and directed at a half-angle of 10–13°, carries a charge of 20–30 nC or 1–2 nC per joule of laser energy within the full half-width of the focal spot [28, 29]. These electrons, passing through high-Z converter, generate bright MeV bremsstrahlung, isotopes and neutrons in photonuclear reactions [5, 31]. The robustness of the DLA mechanism for generating laser-driven particles and radiation was also confirmed in numerous experiments at the PHELIX facility [5, 28–33] with a similar experimental setup to that shown in Fig. 7 in Methods.

To characterize the energy and angular distribution of DLA electrons, optimizing shots at an intensity of 10^{19} W/cm^2 were first performed onto foam backed with a thin foil. Figure 1 shows electron spectra measured along the laser axis for various target configurations and with and without pre-heating by a ns pulse. In all shots, the electron energy distribution can be well described by a quasi-Maxwell distribution with an effective temperature. The light-gray spectrum corresponds to a 50 μm thick Al foil irradiated at a high ns laser contrast of 10^{-11} (shot 4). Its effective electron temperature of 1.4 MeV is in good agreement with the ponderomotive scaling expected for a laser intensity of 2×10^{19} W/cm² [34].

The advantages of the target pre-heated by a ns-pulse preceding the main relativistic pulse in case of a long focusing parabola are evident from the analysis of the electron energy distribution measured in shots on a pre-ionized Al-foil and foams. When the ns pulse of 3 ns duration and 5×10^{14} W/cm^2 intensity, forerunning the main relativistic pulse is applied to the same Al-target as in shot 4, the electron spectrum (black curve, shot 1) exhibits a sevenfold increase in effective electron temperature to ~ 10 MeV, alongside a 25-fold increase in the number of electrons per steradian accelerated in the laser direction. The remaining spectra in the Figure (shots 8, 20, and 21), recorded using various foam targets converted into plasma, consistently show a 10-fold increase in the effective temperature up to 14.2 MeV and a 65-fold increase of the number of electrons per steradian emitted in laser pulse direction compared to results on irradiation of Al-foil at high laser contrast.

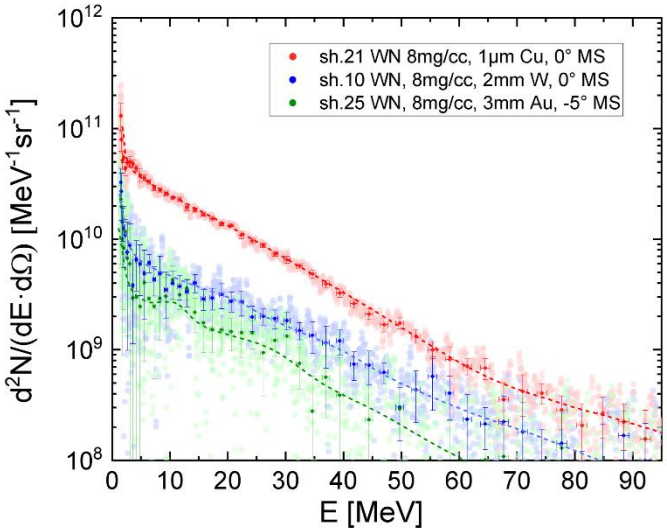
Figure 1: Electron spectra comparison with and without ns-pulse



Electron spectra measured along the laser axis (0°) by 0.99 T magnet spectrometers for different target setups, using high laser contrast with and without ns-pulse: shot 4 (grey curve) - high contrast laser interaction with 50 µm Al-foil; shot 1 (black curve) - laser interaction with 50 µm Al-foil pre-ionized by a ns pulse; shots 8, 20, 21 - laser interaction with foam layers converted to plasma by a ns pulse.

The propagation of electrons in matter is characterized by elastic and inelastic collisions, which lead to energy loss and deceleration of the electrons and production of bremsstrahlung. Figure 2 shows electron spectra measured at 0°/-5° to the laser axis after the DLA electrons, generated in the pre-ionized foam, have left the foam backed by the thin foil (red) and converters (blue, green). This suggests that approximately 20% and less than 10% of the electrons with energies above 7.5 MeV exit the 2 mm and 3 mm high- Z converter, respectively.

Figure 2: Electron spectra after passing different converters



Comparison of energy distribution of direct laser accelerated (DLA)-electrons emerging from the pre-ionized by a ns-pulse foam backed with 1 µm Cu-foil (red), 2 mm thick W (blue) and 3 mm thick Au used as converters.

The 3 mm converter thickness is optimal for conversion of the electron energy into bremsstrahlung in GDR for a given electron energy distribution (Fig. 1), which was also demonstrated by GEANT4 simulations [29].

Based on this analysis, it is expected that the use of low-density foams converted into plasma in combination with high-Z converters will significantly increase the production of MeV bremsstrahlung for various applications.

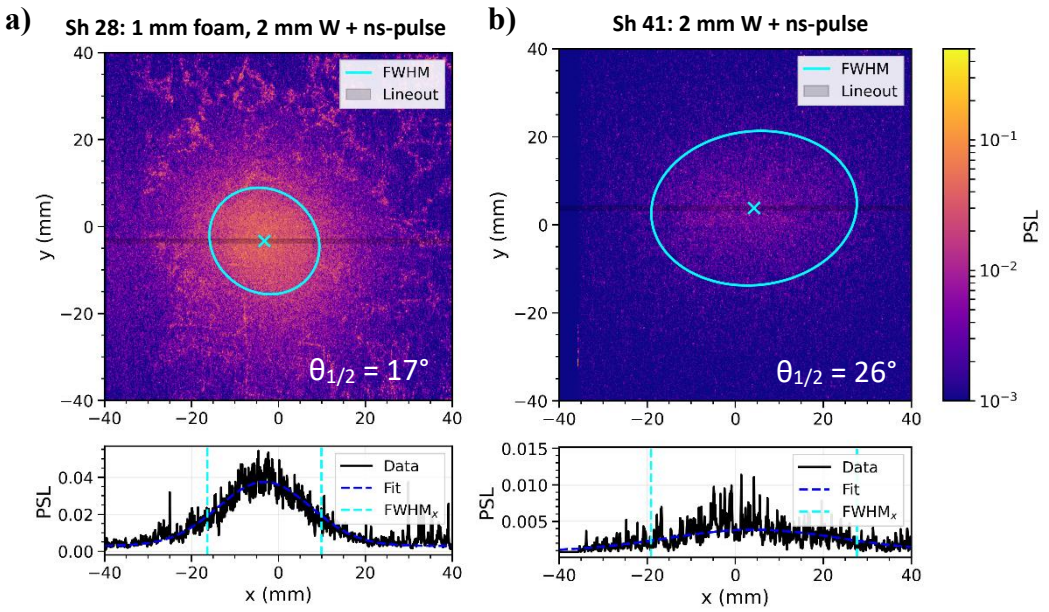
As it was mentioned in the introduction, highly efficient generation of photons with energies between 0.1 and 1 MeV are important for the study of dense, transient states of matter in HED and ICF experiments, while photons in the GDR range, capable of producing isotopes and neutrons, are relevant for laboratory astrophysics.

b) Generation and characterization of MeV bremsstrahlung

In the reported experiment, the spectrum of bremsstrahlung radiation across a broad photon energy range was characterized using a stack of eight thick filters with thermo-luminescence cards (TLD) and imaging plates (IP) as detectors (further referred to as an 8-channel TLD spectrometer). In the GDR photon range, the yields of isotopes of converter materials (e.g., Au, Ta, In) and high-atomic-number probes were analyzed. Autoradiography with gamma-ray-activated copper foils was employed to visualize the spatial distribution of the MeV gamma rays and to verify the beam alignment (see Methods for more details).

Figure 3 shows the divergence of the MeV bremsstrahlung in the energy range of 14–21 MeV, which were generated by a PHELIX shot at a 2 mm tungsten converter placed after the foam layer of 4 mg/cc density and 1 mm thickness (shot 28) a) and by a direct shot at a tungsten converter (shot 41) b). In both cases, a ns pulse was used as a heater before the relativistic main pulse to produce an extended pre-plasma.

Figure 3: Results of autoradiography at a photon energy of 14–21 MeV in shots on foam with converter and converter alone, heated by the ns pulse

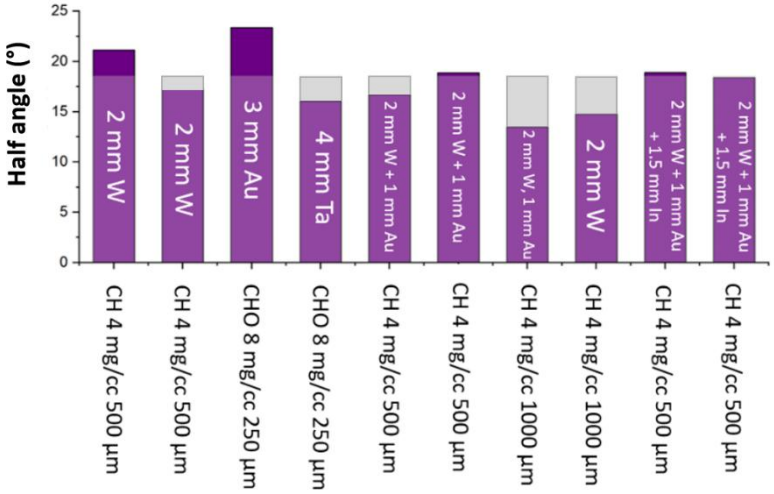


Imaging Plate (IP) scans for different target setups: **a** a shot on foam with a 2 mm tungsten converter (shot 28), resulting in divergence of 17° half-angle at full width at half maximum and **b** a shot on 2 mm tungsten converter alone (shot 41) with 26° divergence of half-angle at full width at half maximum. Both shots utilized a nanosecond pulse.

The use of the foam target resulted in a more collimated beam, with a half-angle at full width at half maximum (FWHM) of 17° compared to 26° for the single tungsten target. The difference between the two setups is even more pronounced in the peak IP signal reflecting the photon fluence within the energy range of the copper peak cross-section (14–21 MeV FWHM), which shows a ratio of approximately 9 to 1. This comparison highlights the significant impact of the foam target on the resulting MeV bremsstrahlung and correlates with the electron spectra shown in Fig. 1, which were measured in shots at pre-ionized Al foil and foam.

Figure 4 presents the half-angle (FWHM) of the gamma-beam cone (14–21 MeV), measured by autoradiography for various target configurations. The results show that the divergence of the MeV beam remains collimated and stable, even when varying the foam parameters and the converter thickness from 2 to 4 mm. This approach thus provides a reliably collimated MeV photon source for diverse applications.

Figure 4: Half-angle divergence at FWHM of the directed MeV bremsstrahlung



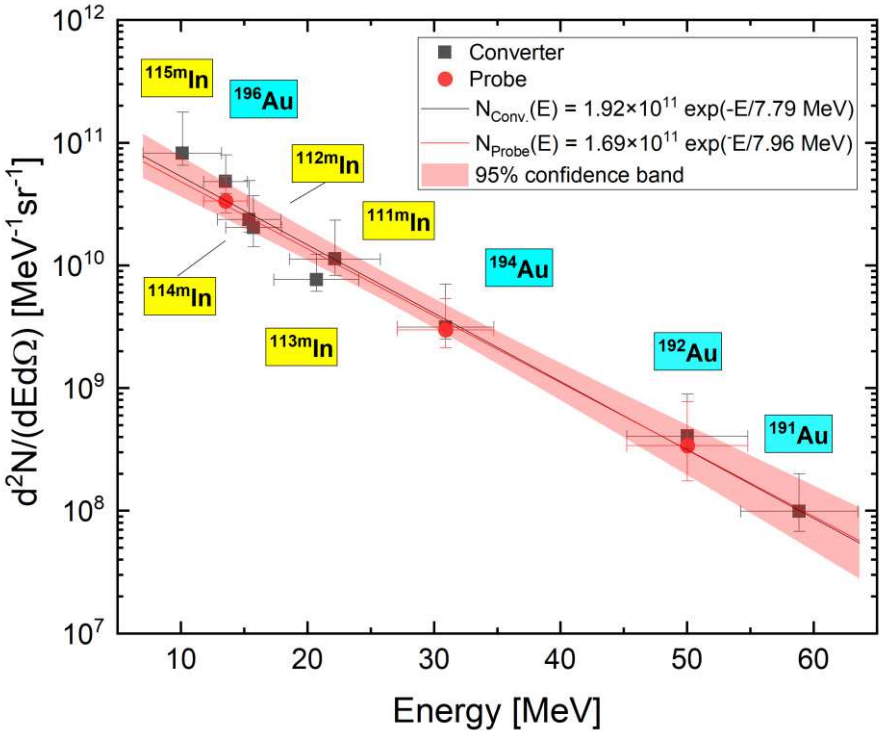
Half-angle at full width at half maximum (FWHM) of the directed bremsstrahlung in 14–21 MeV energy range measured for various target configurations. The converter materials are labeled on the bars and the foam target types specified below. The gray shaded area represents the average value across all shots.

The bremsstrahlung spectrum for the exemplary shot 37 (4 mg/cc 500 µm CH-foam backed with 2 mm W, 1 mm Au and 1.5 mm In) reconstructed using isotopes of Au, Ta and In is shown in Fig. 5. The corresponding number of isotopes produced in this shot can be found in the supplementary material (Table 3). In this shot, the energy of the main laser pulse on target was (65 ± 8) J, and (19 ± 2) J inside the FWHM of the focal spot, with corresponding intensity of 10^{19} W/cm^2. The ns-pulse used to convert foam into plasma delivered 2 J on target within 3 ns, resulting in an intensity of 3×10^{14} W/cm^2. The delay between the ns- and ps-pulses was 5 ns.

Each datapoint in Fig. 5 represents an individual nuclear reaction. Its position on the x-axis is determined by the peak energy of the respective reaction, while the energy error corresponds to the FWHM of the reaction cross section (see Supplementary Fig. 1). The number of photons at the associated energy is calculated by accounting for several factors. These include the number of isotopes measured by high-purity germanium (HPGe) detectors, the reaction cross sections, and the geometric positioning of the probe inside the FWHM of the MeV bremsstrahlung beam as determined via copper autoradiography (see section “Autoradiography”). The isotopes

resulting from these nuclear reactions are labeled directly within the graph. The vertical uncertainty is derived from two primary components. First, it accounts for the statistical uncertainty inherent in the determination of the peaks and counts measured by HPGe detectors from which the data points are reconstructed. Second, it incorporates the aspect that only the portion of the reaction cross section located within the FWHM is taken into consideration for the calculation.

Figure 5: Reconstructed bremsstrahlung spectrum



Bremsstrahlung-spectrum in case of shot 37 with 4 mg/cc 500 µm polymer aerogels consisting of carbon and hydrogen CH-foam target in combination with 2 mm W, 1 mm Au and 1.5 mm In. The main laser pulse delivered (65 ± 8) J to the target, with (19 ± 2) J within the focal spot full width at half maximum (FWHM), reaching an intensity of 10^{19} W/cm^2. To transform the foam into plasma, a 2 J ns-pulse was applied over 3 ns at an intensity of 3×10^{14} W/cm^2, with a 5 ns delay before the arrival of the ps-pulse.

By synthesizing these individual points, the complete spectrum can be reconstructed. For photons above 7.5 MeV, the distribution was fitted with exponential functions with effective temperatures of (7.8 ± 0.4) MeV for the converter: $N_{Ph}(E) = 1.9 \times 10^{11}$ exp (-E/7.8 MeV) ph/sr and (8.0 ± 0.5) MeV for the probe: $N_{Ph}(E) = 1.7 \times 10^{11}$ exp (-E/8.0 MeV) ph/sr.

This results in photon fluences of $(5.7 \pm 0.6) \times 10^{11}$ sr^{-1} (converter), $(5.2 \pm 0.6) \times 10^{11}$ sr^{-1} (probe) and a total photon number of $(1.9 \pm 0.2) \times 10^{11}$ (converter), $(2.1 \pm 0.2) \times 10^{11}$ (probe) within the FWHM of the MeV bremsstrahlung beam cone.

A specific focus was placed on the indium isotopes, which fill the photon energy gap between ^{196}Au and ^{194}Au gap and whose production involves several photon and neutron reaction channels (see Supplementary Fig. 5). Since indium is a primary candidate for neutron diagnostics, careful analysis was required to determine its suitability for bremsstrahlung detection in the region of giant dipole resonance. The cross section of ^{115m}In production by

neutrons is more than 200 times higher than by photons. On the other hand, the highest conversion efficiency of bremsstrahlung to neutrons of 0.02 % was demonstrated in [5]. Another factor that greatly reduces the role of neutrons in ^{115m}In production is the anisotropy (4π) of neutrons resulting from photonuclear reactions. At the same time, the DLA-based MeV bremsstrahlung beam is directed along the laser axis within 0.16–0.20 sr. This leads to a clear dominance of the photon-induced channel when ^{115m}In is measured along the laser axis.

To validate this assumption, the bremsstrahlung reconstruction was performed both with and without the inclusion of indium data. The resulting spectra show minimal deviation, confirming that the indium yield is driven almost entirely by photons rather than neutrons in the case of directed MeV bremsstrahlung beams. Because they align closely with the fit, the underlying approximations are validated. Consequently, multiple indium datapoints could be successfully integrated into the bremsstrahlung spectrum reconstruction, enhancing the statistical weight of the data and reducing the reliance on any single material or reaction.

Characterization of bremsstrahlung using TLD spectrometer

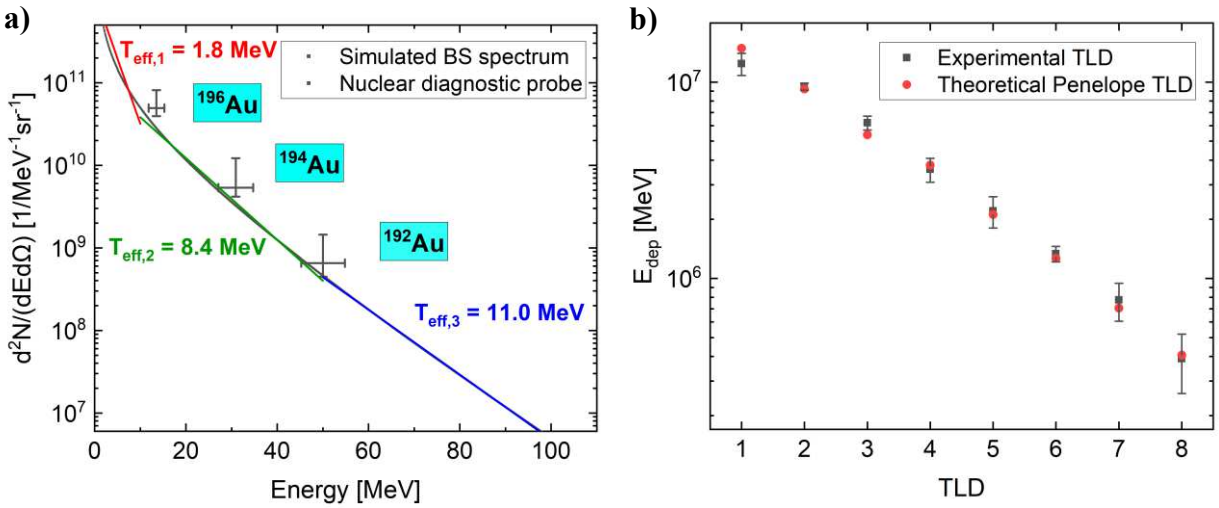
Geant4 [35] simulations were performed to interpret the experimental data obtained by means of 8-channel TLD spectrometer. The real experimental configuration was reproduced, including target composition, as well as detector position. The set of eight thick filters, described in Methods, was reproduced in detail, considering the exact disposition and dimensions of filters, sensitive parts (imaging plate and TLDs) and a lead shielding. The energy deposited by photons and electrons in the sensitive part of the detector was registered as score. Electron spectrometers were simulated considering fictive detectors placed at the right position and angle from the TCC, registering the incident electron spectra. The physics library used in the simulation was Penelope [36]. Electrons were injected at the front side of the converter considering a double temperature Maxwellian distribution.

$$f(E) = N\left(\frac{1}{A}e^{-\frac{E}{T_1}} + \frac{1}{B}e^{-\frac{E}{T_2}}\right)$$

where N is the absolute number of electrons, T_1 and T_2 the temperatures and A and B two normalization factors, in energy units. The values of the coefficients were retrieved through an iterative procedure, by performing an extensive simulation effort, aimed at reproducing the experimental signal collected by the diagnostics (both electron and photon spectrometers). Simulations show that electrons exiting a 3 mm thick converter contribute up to 20% to the TLD dose in the first two channels, while only photons are registered in channels 4 to 8.

Figure 6a shows a bremsstrahlung spectrum, which provides a good agreement between the simulated energy deposition in the each of the eight TLDs and the experiment in shot 30. Here, the target setup consisted of 4 mg/cm^3, 1 mm thick CH foam, 2 mm W and 1 mm Au as a converter. The bremsstrahlung spectrum can be described by an exponential function with three effective temperatures: T_1 = 1.8 MeV (E_{ph} < 10 MeV), T_2 = 8.4 MeV (GDR) and T_3 = 11.0 MeV (E_{ph} > 50 MeV).

Figure 6: Comparison of reconstructed MeV-bremsstrahlung between ND- and TLD-results



a: Simulated bremsstrahlung spectrum, which provides a good agreement with thermoluminescent dosimeter (TLD) signal in all eight channels together with a photon fluence at selected photon energies as a result of photo-nuclear reactions in gold. The spectrum can be described by an exponential function with three effective temperatures: T_1 = 1.8 MeV (E_{ph} < 10 MeV), T_2 = 8.4 MeV (giant dipole resonance) and T_3 = 11.0 MeV (E_{ph} > 50 MeV);
b: Comparison between simulated and experimental energy deposition by electrons and photons into each TLD.

In the energy range of 0.1–1 MeV, the estimated photon fluence for a 3 mm thick converter reaches 5×10^{12} ph/sr. According to Monte Carlo simulations, a converter thickness of 1 mm is more advantageous for this photon energy range, as it leads to a reduction in self-absorption and a doubling of the photon fluence.

The photon fluences in the GDR, determined from the yields of ^{196}Au, ^{194}Au and ^{192}Au at selected photon energies and the resulting effective temperature of 8.3 MeV (E_{ph} > 7.5 MeV) show good agreement with the TLD-diagnostic. The integrated fluence of photons above 7.5 MeV results in $(4.9 \pm 0.1) \times 10^{11}$ ph/sr in case of TLD diagnostics and in $(8.2 \pm 0.8) \cdot 10^{11}$ ph/sr in case of ND.

The calculated conversion of the laser energy into photons above 7.5 MeV for TLD is (1.1 ± 0.2) % compared to (1.8 ± 0.3) % in case of ND. It should be noted that the reaction cross sections at FWHM in the corresponding energy range were used in the evaluation of the photon spectrum based on the activation results. Consequently, the number of photons within the FWHM of the gamma-ray profile and the laser energy within the FWHM of the focal spot were used to estimate the conversion efficiency.

Simulations were performed to determine the energies of DLA electrons with exponentially decaying spectra, which contribute significantly to the formation of the bremsstrahlung spectrum in Fig. 6. It was shown that electrons with energies of 0–10 MeV contribute only about 3% to the overall spectrum, those with energies of 30–60 MeV about 25%, and those with energies of 60–100 MeV about 12%. The remaining approximately 60% is caused by DLA-electrons with energies of 10–30 MeV.

In order to evaluate the angular divergence of the photon beam in GEANT-4 simulations, spherical coronas of 1 rad were implemented as sensitive detectors, covering the half solid angle. These detectors scored the number of photons that impinged on them, providing a synthetic signal to be compared with the experimental data collected by the diagnostic. According to simulations, the divergence (FWHM/2) of 100 keV photons is 31.8°, of 1–5 MeV 15.3° and of 10 MeV 13°, compared with 17–20° measured by autoradiography.

3. Methods

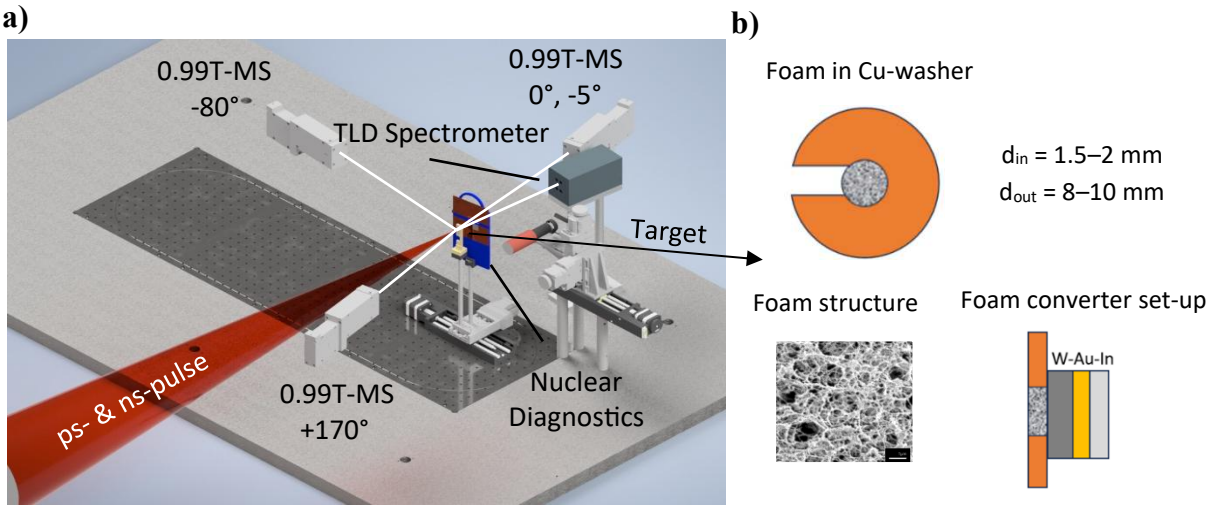
The experiment was performed using 200 TW Nd: glass PHELIX laser [25, 26] at an intensity of ~ (1–2) x 10^{19} W/cm² and a total average energy on target of (60 ± 8) J. A laser pulse of (750 ± 250) fs duration was focused on target using a 150 cm off-axis parabolic mirror to a spot of (15 ± 2) μm, measured at the FWHM. The laser energy within the FWHM was estimated to be (17 ± 2) J.

In the experiment, low-density (2–8 mg/cm³) polymer foams (consisting of CHO and CH) of 0.25–1.0 mm thickness backed with a thin metallic foil or with the mms-thick high-Z converter were used as targets. A nanosecond pulse with controlled energy and duration, preceding the relativistic main pulse, was focused on the target using the same parabolic mirror as a picosecond pulse to convert the foam into plasma. The relativistic short pulse was directed onto the plasma target with a delay of 3–5 ns and triggered the direct laser acceleration of electrons [28–30].

The diagnostic and target set-ups are presented in Fig. 7a, b. The direction of ns and ps laser beams focused on the target by the same f/5 of-axis parabolic mirror is shown schematically in red. The PHELIX laser system delivers high energy shots every 90minutes.

For measurements of the electron energy distribution at 0° or -5°, 80° and 170° to the laser axis, a set of 0.99T magnet spectrometers (MS) charged with Imaging Plates (IP) was used. The angular distribution of electrons with energies beyond 3.5 and 7 MeV, was measured by means of IPs placed between three 3 mm thick stainless-still cylindrical plates (not shown in the scheme), see for more details [29]. Figure 7b shows a foam layer grown inside a Cu ring, the foam microstructure and the foam- converter set-up.

Figure 7: Experimental setup at the PHELIX facility



The schematic illustration of the experimental and the target setups with the laser beam in red and three magnet spectrometers (MS) arranged at angles of -80°, forward direction (0° or -5°), and +170°. Additionally, the setup includes 8-channel thermoluminescent dosimeter (TLD) spectrometers placed along the laser axis. The right side shows a polymer aerogel consisting of carbon, oxygen and hydrogen (CHO) foam target grown in a copper ring, along with its microstructure [27]. The target set-up consists of the foam layered with 2 mm of tungsten, 1 mm of gold, and 1 mm of indium. The laser pulse heats the target from the left.

Autoradiography

To measure the divergence of the MeV bremsstrahlung, its spatial distribution and its position relative to the laser axis, copper foils were utilized for autoradiography during the experiment. The bremsstrahlung generates in ^{63}Cu the radioactive isotope ^{62}Cu, which decays to ^{62}Ni with a half-life of 9.74 minutes, emitting 511 keV, 1172 keV photons (0.34%) as well as positrons (98%). The positron energy distribution is peaking at 1320 keV and extending up to 2936 keV (see Supplementary, Fig. 2). To perform autoradiography [37, 38], thin copper foils were placed 2.7–4.0 cm downstream of the TCC.

After laser shot, the activated copper plates were placed on BAS-IP MS imaging plates [39] for 15 minutes. Once scanned, the IP provides a two-dimensional image that can be used for further analysis of MeV bremsstrahlung angular distribution. The threshold energy for the ^{63}Cu(γ, n)^{62}Cu reaction is 10.8 MeV, with the FWHM of the cross-section ranging between 14 and 21 MeV (see Supplementary, Fig. 2). In the case of a 50–100 µm thin Cu foil, where positron annihilation can be neglected, and due to the low IP response to hard X-rays compared to MeV electrons [39], we can attribute the measured IP signal to positrons. Figure 2 (Supplementary) displays the experimentally determined cross-section for this reaction along with a corresponding Lorentz fit.

Figure 8: Autoradiography for MeV bremsstrahlung using activation in copper

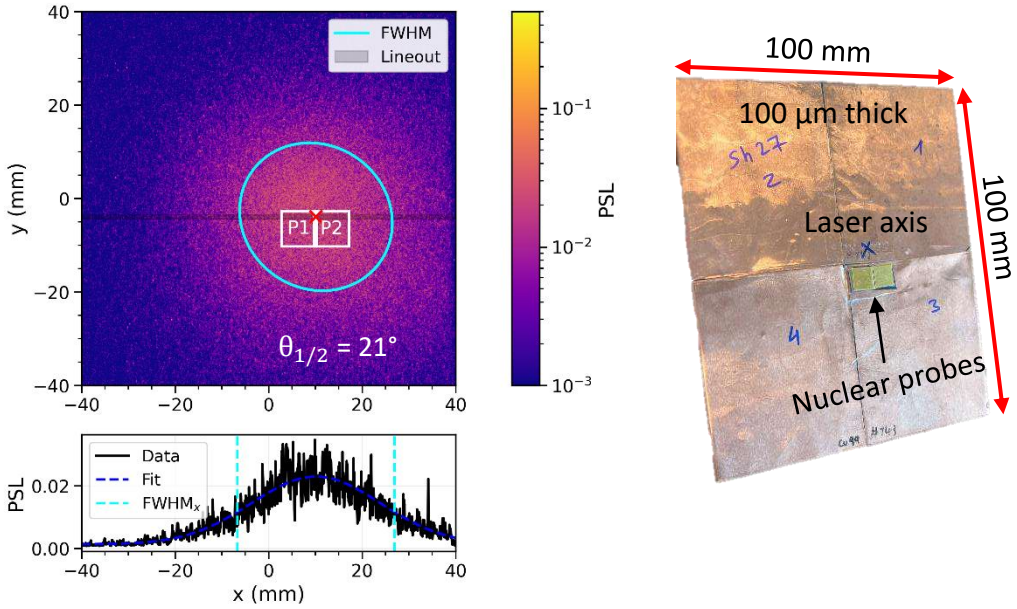


Image Plate (IP) scan of an activated copper foil providing a two-dimensional spatial distribution of the 14–21 MeV bremsstrahlung and the position of the nuclear probe relative to the MeV bremsstrahlung axis. The intensity profile displays the beam divergence of 20° half-angle at full width at half maximum (FWHM). intensity distribution and probe alignment captured here were utilized to correct the photon flux in the bremsstrahlung reconstruction. The right side displays the nuclear diagnostics, consisting of four copper plates (50x50 mm² each, thickness of 100 µm) with two gold probes with dimensions of 7.5x7.5 mm² and 1 mm thickness on top.

Nuclear diagnostics

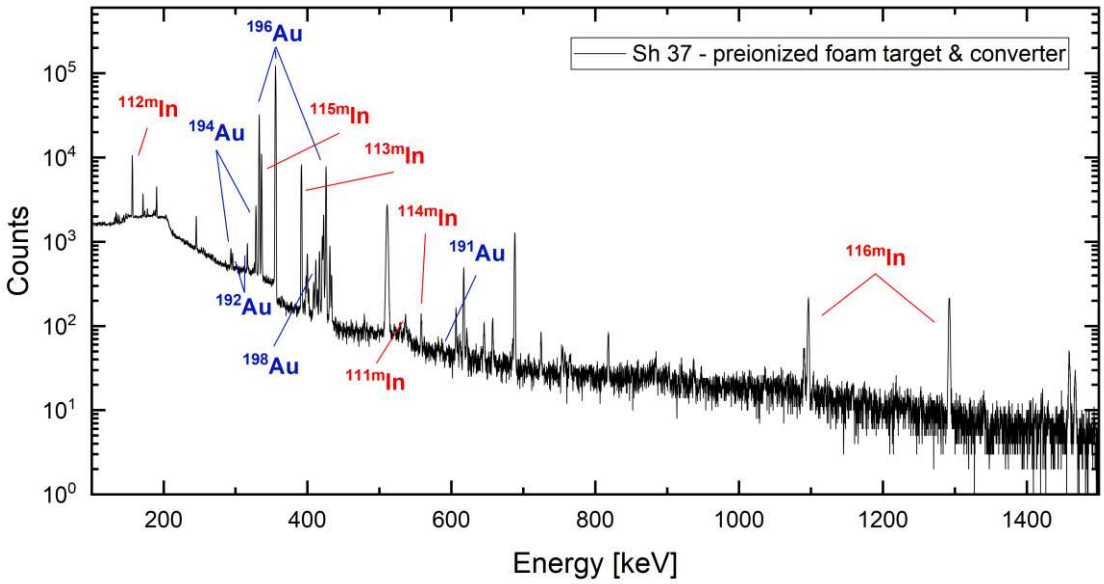
The energy distributions of photons with energies >7.5 MeV, resulting from MeV bremsstrahlung generated by DLA electrons in the converter, were characterized using nuclear diagnostic (ND) methods. This involved analyzing isotope production within Au, Ta and In samples. Following each laser shot, the isotope yields in the activated samples were monitored using HPGe detectors. Fig. 3 presents the gamma ray spectrum collected during 15.08 h by the HPGe detector for shot 37 with 4 mg/cc 500 µm CH-foam and converter consisted of 2 mm tungsten followed by 1 mm gold and 1.5 mm indium.

The identified peaks correspond to the isotopes releasing the photons with distinct energy lines. In this particular spectrum, gold-isotopes up to ^{191}Au have been detected, which corresponds to the reaction ^{197}Au(γ, 6n)^{191}Au at 58.9 MeV peak cross section energy. Accordingly, several indium isotopes were identified. The photon energies necessary to induce these nuclear reactions are listed in Fig. 1 of the Supplementary. In addition to the photon-nucleus reaction with the release of neutrons, neutron capture in Au and In was also observed, producing ^{198}Au and ^{116m}In.

The quantitative analysis of these lines allows for a reliable reconstruction of the underlying bremsstrahlung distributions. As with all spectra presented in this work, the reconstruction incorporates the geometric positioning of the probe relative to the MeV bremsstrahlung beam.

This is achieved by applying the spatial distribution and divergence profiles derived from the copper autoradiography measurements discussed in the previous section.

Figure 9: Photon spectrum for converter material measured with HPGe detector, between 100 keV and 1500 keV



Photon spectrum for a shot (37) using a 4 mg/cc 0.5 mm thick foam target and a converter consisting of 2 mm W followed by 1 mm Au and 1.5 mm In. The acquisition time was 15.08 h. Several characteristic lines of gold and indium isotopes are shown. The presence of ^{191}Au confirms the occurrence of (γ, 6n)-reactions, indicating photon production around 60 MeV within the Au-converter. The detection of ^{116m}In and ^{198}Au identifies neutron-induced reactions, in contrast to the other gamma-produced isotopes.

TLD spectrometer

Another approach to measure and reconstruct the bremsstrahlung spectra in the photon energy range from 30 keV up to 100 MeV is based on application of an array of thick absorbing filters, thermoluminescent detectors (TLD) and imaging plates (IP), capable of measuring doses in the range from 10 µGy up to 10 Gy. The basics of such a spectrometer are described in [28, 40, 41]. In the discussed experiment, a modified portable TLD spectrometer with 8 channels was constructed to be placed inside the vacuum chamber. The following set of filters was used: three Cu-plates with thicknesses of 6, 9 and 10 mm, followed by Fe with thicknesses of 14.5, 19 and 20 mm, Pb with a thickness of 6 mm and PVC with a thickness of 10 mm. The spectrometer was shielded by a 1 cm thick lead casing.

High-energy photons penetrating high-atomic-number materials are not only absorbed but also cause an electromagnetic shower of secondary particles and radiation. In this case, reconstructing the photon spectrum requires Monte Carlo simulations [42] that consider all the physical processes involved, as well as the materials and the geometry of the experimental setup.

4. Summary

This work demonstrates the highly efficient generation of ultra-intense MeV bremsstrahlung radiation using the 200 TW PHELIX laser system. By utilizing optimized foam targets which were pre-ionized by a nanosecond pulse, direct laser acceleration was initiated via a delayed sub-picosecond pulse of moderate relativistic intensity of 10^{19} W/cm^2. This process created a high-current, well-collimated beam of super-ponderomotive electrons that produced intense bremsstrahlung within high-Z converters. The spectral characteristics of generated MeV bremsstrahlung were evaluated using two different methods: by analyzing the absorption in thick filter stack and using nuclear activation methods, specifically targeting photo-nuclear reactions in gold, tantalum, and indium. In the GDR photon energy range (> 7.5 MeV), photonuclear reaction channels in gold up to (γ,6n) were observed, indicating photon energies extending to 60 MeV, obtained at 10^{19} W/cm^2 laser intensity. The divergence of the MeV bremsstrahlung directed along the laser axis, measured using the activation of Cu foil, reached 0.17–0.2 sr. This contrasts with measurements carried out at NOVA [18] and at ARC/NIF [43] which showed a 10-fold greater divergence of ~ 2 sr.

A significant finding of this study was the successful integration of indium into the bremsstrahlung reconstruction. Although indium is sensitive to neutron-induced reactions, our analysis demonstrated that the observed reaction yields were heavily photon-dominated under conditions of directed MeV bremsstrahlung. This allowed for the reliable use of indium as a supplementary diagnostic for photon flux, strengthening the statistical power of the spectral reconstruction. These nuclear diagnostic results were further confirmed by TLD measurements, which showed good agreement in both the fitted effective temperature and the overall spectral shape when compared to the nuclear-reconstructed spectra.

Our analysis confirmed that the DLA-based approach using pre-ionized low-density foams provides a nearly 10-fold increase in photon fluence compared to only converter irradiated by a ns-pulse to generate an extended pre-plasma. This can be explained by a much longer plasma scale length in case of foams, which ensures effective DLA [30].

Using pre-ionized foams and high-Z converters, we demonstrated an ultra-high photon fluence of 10^{13} ph/sr in case of optimized converter thickness for 0.1–1 MeV photons (TLD), which is suitable for radiographic applications in HED and ICF experiments. In the GDR-range (> 7.5 MeV), which is important for the production of isotopes and neutrons in gamma-driven nuclear reactions, the photon fluence of 8×10^{11} ph/sr was obtained using ND-method. Here, the bremsstrahlung spectrum was approximated by an exponential function with effective temperatures 8.4 MeV and 11.0 MeV.

In the following Table 1, we compare the performance of the PHELIX setup with 60 J laser energy and 10^{19} W/cm^2 intensity on target against several high-energy laser facilities including Omega-EP (1.5 kJ, 10^{19} W/cm^2), NOVA (500 J, 3×10^{20} W/cm^2), VULCAN (25 J, 10^{19} W/cm^2), and Titan (120 J, 3×10^{19} W/cm^2). The data focuses on photon fluence in two critical energy windows: 0.1–1 MeV for radiographic applications and GDR (> 7.5 MeV) for nuclear physics.

While absolute photon fluence depends on laser energy, the data are also normalized to the laser energy on target.

Table 1: Comparison of photon fluences generated at PHELIX versus other laser facilities

Laser system	Target set up	0.1–1 MeV		>7.5 MeV (GDR)	
		N_{Ph} [sr^{-1}]	N_{Ph}/E [$sr^{-1}J^{-1}$]	N_{Ph} [sr^{-1}]	N_{Ph}/E [$sr^{-1}J^{-1}$]
PHELIX (60 J) (this work)	foam + converter ns-pulse	~$5x10^{12}$	~$8x10^{10}$	~$8x10^{11}$	~$1.5x10^{10}$
Omega-EP (1.5 kJ) [20]	converter + ns-pulse	~$5x10^{13}$	~$3x10^{10}$	~$2x10^{12}$	~$2x10^{9}$
NOVA (500 J) [18]	converter + ns-ASE	-	-	~$2x10^{11}$	~$4x10^{8}$
VULCAN (25 J) [19]	converter + ns-ASE	-	-	~$2x10^{5}$	~10^{4}
Titan (120 J) [1, 17]	gas-jet + converter	~10^{12}	~10^{10}	-	-

The comparison of the photon fluence generated per joule of laser energy on target in experiments performed at different laser facilities at intensities of 10^{19} W/cm^2 and above demonstrates the clear superiority of our target set-up - the combination of pre-ionized low-density foams with a high-Z converter. This significant increase in bremsstrahlung efficiency opens new possibilities also for high-flux neutron generation and other photo-nuclear applications.

The outstanding properties of pre-ionized foams, which enable efficient electron acceleration even with highly imperfect and large laser focus and near relativistic intensities, were recently demonstrated at PHELIX by artificial defocusing of the laser spot and within the NIF discovery program by shooting foams with the Advanced Radiographic Capability (ARC) laser.

Funding

This work was supported by the Helmholtz Forschungsakademie Hessen für FAIR (HFHF) under contract No. HFHF 2.6.4.2.2 TP, the German Ministry for Education and Research (BMBF) under contract No. 05P21SJFA2 and the Grant Agency of the Czech Republic (Project No. GM23-05027M).

Acknowledgements

Results presented here are based on the experiment P21-5 (2022), which was performed at the GSI Helmholtzzentrum fuer Schwerionenforschung, Darmstadt (Germany) in the context of FAIR Phase-0. We thank the PHELIX team for their continuous support in preparing and conducting our experiment. Special thanks go to General Atomics, Wigen Nazarov and Dieter H. G. Schneider for providing the foam targets. Additional thanks are extended to the Institute for Applied Physics (IAP) at Goethe University Frankfurt for financial support regarding the first author's participation in the experiment. Linguistic refinements to the manuscript were assisted by Gemini 3 Flash. The authors acknowledge support by the Open Access Publication Fund of Goethe University Frankfurt.

Supplementary Material

Nuclear Diagnostics

The core idea behind nuclear diagnostics (ND) is to trigger photo-nuclear reactions in various materials that exhibit resonances in different photon energy ranges leading to isotope production. To identify and quantify the produced isotopes, the samples are measured via High-Purity Germanium (HPGe) detectors with background measurements being performed and accounted for during analysis.

To calculate the number of reactions ($N_{reactions}$) occurring within the sample, we use the following formula [44]:

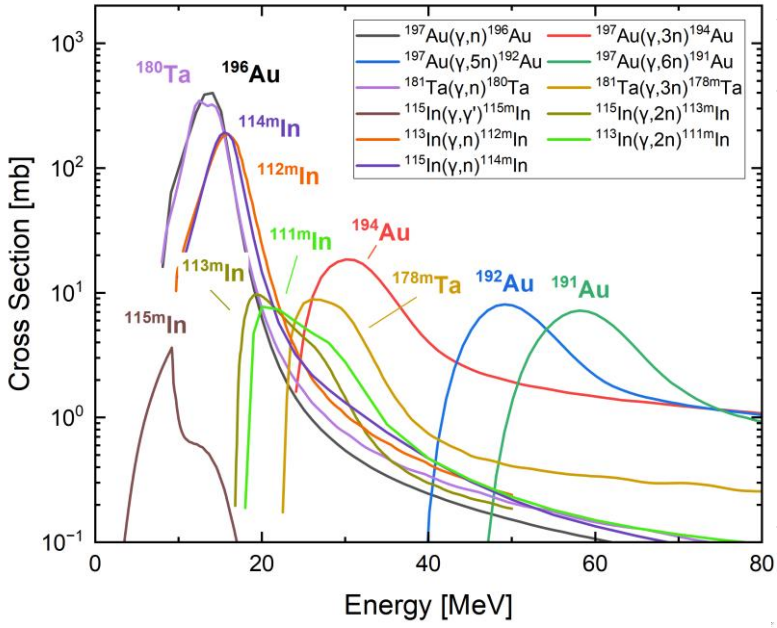
$$N_{\mathrm{reactions}} = \int_{E_{Th}}^{\infty} N_{\mathrm{T}} N_{\mathrm{Ph}}(E)\sigma(E)\ dE$$

where:

- $N_{reactions}$ is the number of reactions, corresponding to the number of isotopes produced via a specific reaction-channel.
- N_{T} represents areal density of the target atoms within the sample.
- $N_{\mathrm{Ph}}(E)$ is the photon number per energy of the incoming MeV bremsstrahlung.
- $\sigma(E)$ denotes the energy-dependent reaction cross-section.
- The integral spans from the lower threshold energy E_{Th} of the reaction up to infinity (or the maximum available data).

In order to reconstruct the bremsstrahlung spectrum for each shot using this formula, precise knowledge of the energy-dependent reaction cross sections for each isotope produced is required. The reactions primarily occur within the giant dipole resonance (GDR). Supplementary Fig. 1 provides an overview of the cross sections for various elements used in the experiment. The accompanying table contains the peak energies and full width at half maximum of the photonuclear cross-section.

Supplementary Figure 1: Cross-sections of nuclear reactions for MeV bremsstrahlung

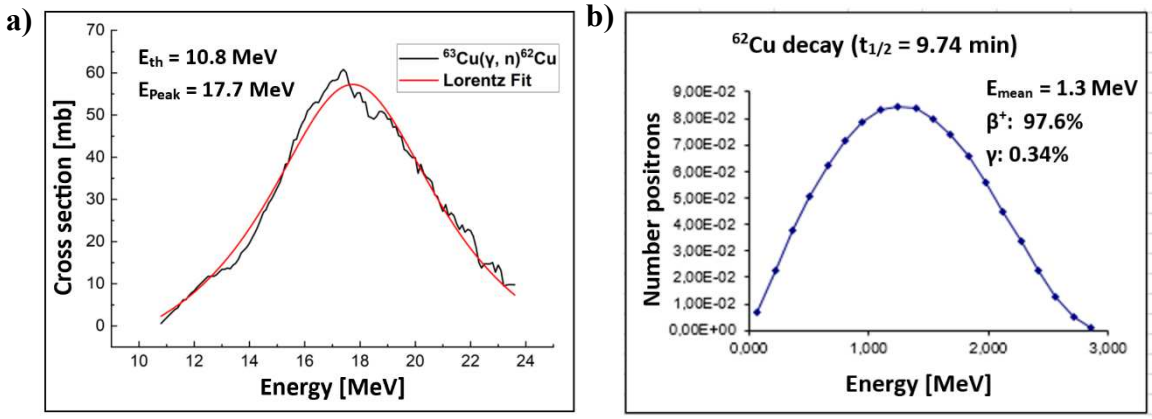


Reaction	E_{Peak} / MeV	FWHM / MeV
^{197}Au(γ, n)^{196}Au	13.54	3.48
^{197}Au(γ, 3n)^{194}Au	30.92	7.64
^{197}Au(γ, 5n)^{192}Au	50.04	9.56
^{197}Au(γ, 6n)^{191}Au	58.87	10.91
^{181}Ta(γ, n)^{180}Ta	13.26	4.07
^{181}Ta(γ, 3n)^{178m}Ta	27.50	7.43
^{115}In(γ, γ')^{115m}In	10.12	2.78
^{115}In(γ, n)^{114m}In	15.40	4.24
^{115}In(γ, 2n)^{113m}In	20.72	6.72
^{113}In(γ, n)^{112m}In	15.75	4.41
^{113}In(γ, 2n)^{111m}In	22.18	7.19

Photonuclear reaction data used for spectral reconstruction. The left panel shows the cross-sections of various reactions as a function of photon energy, highlighting the probability of generating different isotopes across the energy spectrum. The right panel provides a corresponding table that summarizes the specific nuclear reactions, including their respective peak energies and the full width at half maximum (FWHM) of the resonance peaks [45].

The underlying physics for the autoradiography in copper is shown in Supplementary Fig. 2. The cross section for the reaction in natural copper is displayed in part a), while b) shows the energy distribution of the positrons emitted during ^{62}Cu decay. These characteristics are important to identify the MeV-beam angular distribution and its location relative to the laser axis.

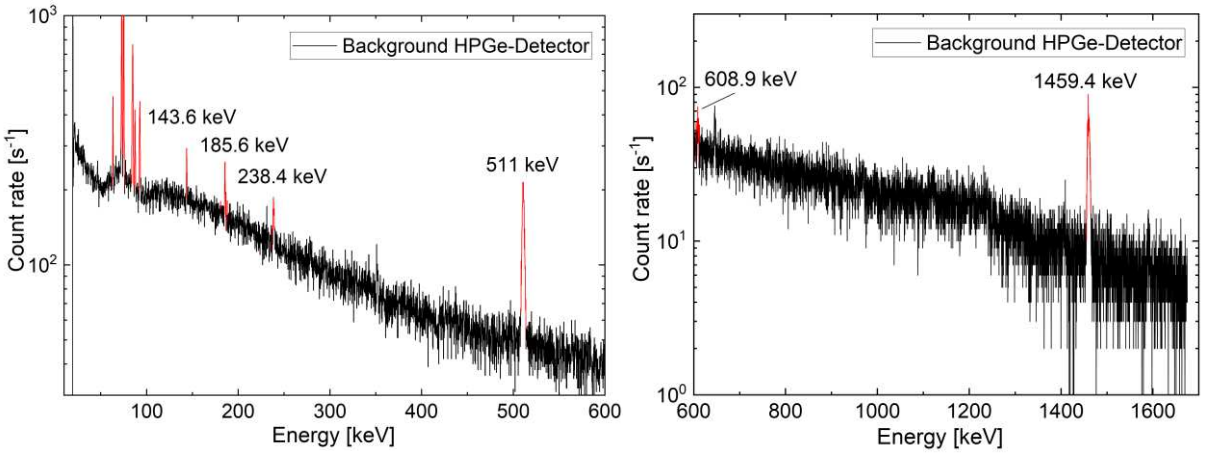
Supplementary Figure 2: Copper nuclear reaction cross-section and ^{62}Cu positron distribution for autoradiography



a: Profile of the experimentally determined cross-section for the reaction (black) and the corresponding fit (red) [45].
b: Profile of the positron energy distribution in blue. Initial positron energies were defined based on the available beta-ray spectrum data for ^{62}Cu, taken from the MCNP code [46].

Background measurements

Supplementary Figure 3: Background measurement for HPGe detectors



Energy spectra of the background measurement for the detectors used in two energy ranges. The most prominent lines are marked in red and labeled with their respective energies.

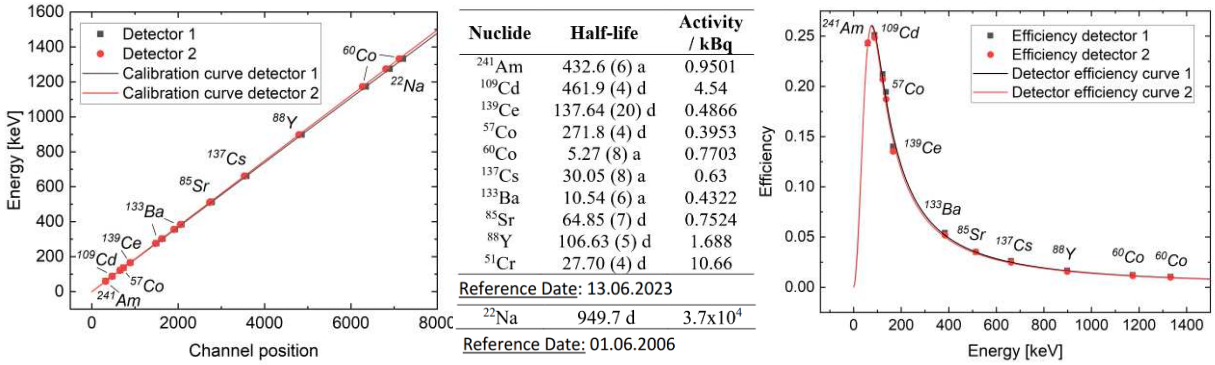
Supplementary Table 1: The table lists the energy lines and the corresponding isotopes identified during the background measurement, along with the measured counts per second for each peak.

Energy / keV	Isotope	Countrate / 10^{-3} s^{-1}
63.4	^{234}Th	1.36 ± 0.12
72.7	^{235}U	5.44 ± 0.20
75.0	^{235}U, ^{212}Pb	14.60 ± 0.29
84.9	Pb $K_{\beta1}$, Pb $K_{\beta3}$	6.07 ± 0.24
87.2	^{212}Pb	2.35 ± 0.19
92.6	^{234}Th	2.44 ± 0.17
143.6	^{235}U	1.12 ± 0.18
185.6	^{235}U	1.42 ± 0.19
238.4	^{212}Pb	1.12 ± 0.23
351.9	^{214}Pb	0.46 ± 0.15
511	Annihilation, ^{222}Rn	7.58 ± 0.70
608.9	^{214}Bi	0.99 ± 0.25

Detector Calibration

Supplementary Fig. 4 provides a detailed illustration of the energy calibration on the left and the efficiency calibration on the right. For this calibration, a mixed radionuclide source was employed in conjunction with a ^{22}Na-source. The specific isotopes, their respective half-lives and activities at the reference date are also listed in the Supplementary Fig. 4.

Supplementary Figure 4: Energy and efficiency calibration for the HPGe detectors



Nuclide	Half-life	Activity / kBq
^{241}Am	432.6 (6) a	0.9501
^{109}Cd	461.9 (4) d	4.54
^{139}Ce	137.64 (20) d	0.4866
^{57}Co	271.8 (4) d	0.3953
^{60}Co	5.27 (8) a	0.7703
^{137}Cs	30.05 (8) a	0.63
^{133}Ba	10.54 (6) a	0.4322
^{85}Sr	64.85 (7) d	0.7524
^{88}Y	106.63 (5) d	1.688
^{51}Cr	27.70 (4) d	10.66
Reference Date: 13.06.2023		
^{22}Na	949.7 d	3.7x10^{4}
Reference Date: 01.06.2006		

Calibration results for the high purity germanium (HPGe) detectors. Left: Energy calibration curves with associated isotopes. Middle: Table of radioactive isotopes used for calibration. Right: Detection efficiency curves with associated isotopes.

Nuclear cross sections within resonance peak

After every laser shot, the yield of generated isotopes was measured, having resonances at different photon energies, using high purity germanium (HPGe) detectors. This allows to accurately reconstruct the energy distribution of the incoming MeV photons.

Accurate interpretation of the experimental data using the High Purity Germanium (HPGe) detectors required comprehensive calibration. This process involved two main steps: first, establishing the precise energy-to-channel position relationship, and second, characterizing the detector's energy-dependent photon detection efficiency.

The relationship between energy and channel position is largely linear. The detection efficiency curve shows a more complex dependency. The efficiency initially rises steeply at lower energies, reaching its peak at approximately 25% within the energy range below 200 keV. Following this maximum, it exhibits a sharp decrease, which then transitions into a more gradual, asymptotic decline. The efficiency is reduced to only a few percent at higher energies (above 1 MeV).

Supplementary Table 2: Characteristics of the detected nuclear reactions, including their threshold and peak energies, the average cross section per MeV calculated within the peak's full width at half maximum (FWHM), and the correction ratios applied to account for the cross section outside of the FWHM range.

Reaction	E_{Thresh} / E_{Peak} [MeV]	FWHM [MeV]	$< \sigma >$ [mb]
$^{197}Au(\gamma, n)^{196}Au$	8.1 / 13.54	3.48	341.89
$^{197}Au(\gamma, 3n)^{194}Au$	24.1 / 30.92	7.64	16.11
$^{197}Au(\gamma, 5n)^{192}Au$	39.1 / 50.04	9.56	6.82
$^{197}Au(\gamma, 6n)^{191}Au$	46.1 / 58.87	10.91	5.89
$^{181}Ta(\gamma, n)^{180}Ta$	8.0 / 13.26	4.07	298.48
$^{181}Ta(\gamma, 3n)^{178m}Ta$	22.5 / 27.50	7.43	7.73
$^{115}In(\gamma, \gamma')^{115m}In$	1.3 / 10.12	2.78	6.74
$^{115}In(\gamma, n)^{114m}In$	9.3 / 15.40	4.24	660.2
$^{115}In(\gamma, 2n)^{113m}In$	16.8 / 20.72	6.72	49.8
$^{113}In(\gamma, n)^{112m}In$	9.7 / 15.75	4.41	660.94
$^{113}In(\gamma, 2n)^{111m}In$	17.7 / 22.18	7.19	32.6

The yields for shot 37 (4 mg/cc 500 µm CH-foam backed with 2 mm W followed by 1 mm Au and 1.5 mm In) for gold and indium isotopes measured both for the 1 mm Au and 1.5 mm In as last layers of the converter and the probes placed 30 mm apart TCC along the laser axis, are presented in Supplementary Table 3. For detailed information about the reaction channels, including their specific thresholds, peak cross-section energies, and widths, see Supplementary Table 2.

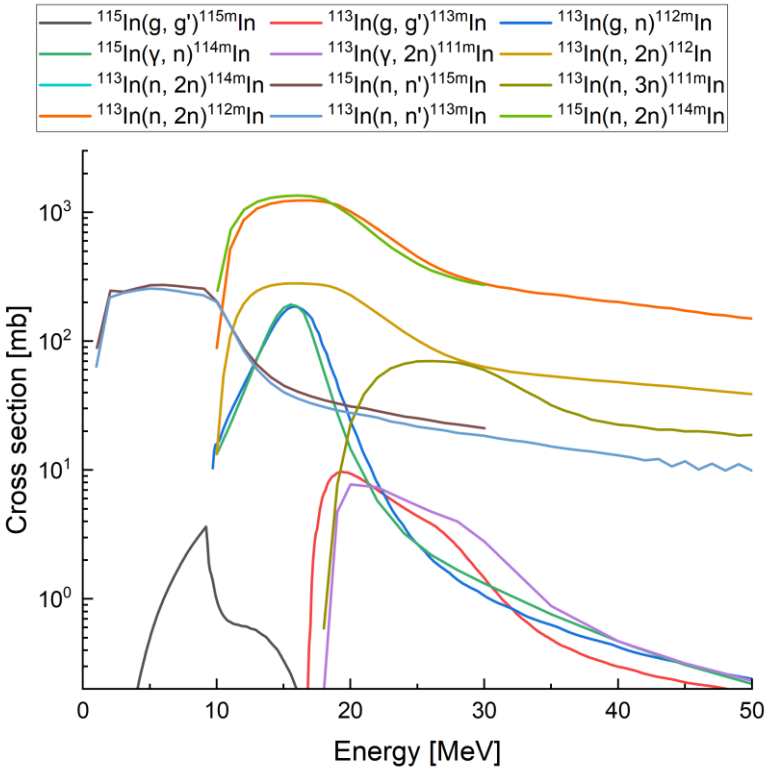
Supplementary Table 3: Measured yields of various Au and In isotopes for shot 37, comparing the activation of the converter and the probe at 40 mm distance. The table lists the number of isotopes for Au from ^{198}Au down to ^{191}Au and for indium from ^{116m}In down to ^{111m}In.

Isotope	Sh 37 yield converter	Sh 37 yield probe
^{198}Au	$4.50 \cdot 10^5$	-
^{196}Au	$2.46 \cdot 10^8$	$2.27 \cdot 10^6$
^{194}Au	$1.62 \cdot 10^6$	$2.03 \cdot 10^4$
^{192}Au	$1.14 \cdot 10^5$	$1.26 \cdot 10^3$
^{191}Au	$2.79 \cdot 10^4$	-
^{116m}In	$3.69 \cdot 10^5$	-
^{115m}In	$2.21 \cdot 10^6$	$7.59 \cdot 10^4$
^{114m}In	$6.25 \cdot 10^7$	-
^{113m}In	$1.53 \cdot 10^6$	$7.92 \cdot 10^4$
^{112m}In	$3.63 \cdot 10^6$	$1.46 \cdot 10^5$
^{111m}In	$6.61 \cdot 10^4$	-

The difference in the measured isotope yields between the converter and the probe is explained primarily by the geometry of the ND set-up and thickness of activation probes. The Au and In parts of the converter is in immediate proximity to the gamma source (2 mm W) and therefore collects the entire photon flux.

In contrast, the Au- and In-probes (Au: 10×10 mm^2, 50 µm thickness; In: 15×15 mm^2, 0.5 mm thickness) placed at 30 mm placed at 30 mm distance from the target cover a much smaller solid angle and have smaller areal density compared to the Au converter of 1 mm thickness.

Supplementary Figure 5: Cross section for nuclear reactions in Indium



Overview of the cross sections for several photonuclear and neutron-induced reaction channels in indium of several isotopes. These data provide a basis for distinguishing between activation caused by the bremsstrahlung spectrum and the neutron flux [45].

Author contributions

SB, PT, and OR wrote the manuscript and conceived the experimental project; SB and PT developed nuclear diagnostic and evaluated results; US provided hands-on support for the setup and operation of the HPGe detector system; MG conducted measurements of DLA electrons; EK and AT were responsible for TLD diagnostic and GEANT4 simulations; MG, PB, PT, and OR were involved in the shot preparation, data collection, and data analysis; NA, CS and JJ were responsible for revising the work critically.

Conflict of Interest:

The authors declare that the research was conducted in the absence of any commercial or financial relationships that could be construed as a potential conflict of interest.

References

1. King M, Lemos N, Shaw JL, Milder AL, Marsh KA, Pak A, et al. X-ray analysis methods for sources from self-modulated laser wakefield acceleration driven by picosecond lasers. Rev Sci Instrum (2019) 90:033503. doi:10.1063/1.5082965

2. Berman BL, Fultz SC. Measurements of the giant dipole resonance with monoenergetic photons. *Rev Mod Phys* (1975) 47:713. doi:10.1103/RevModPhys.47.713

3. Vallières S, Fillion-Gourdeau F, Fourmaux S, Poupart B, Raîche ND, Nicholas F, et al. High average-flux laser-driven neutron source. *Nat Commun* (2025) (in press). doi:10.1038/s41467-025-66535-9

4. Pomerantz I, McCary E, Meadows AR, Arefiev A, Bernstein AC, Chester C, et al. Ultrashort Pulsed Neutron Source. *Phys Rev Lett* (2014) 113:184801. doi:10.1103/PhysRevLett.113.184801

5. Günther MM, Rosmej ON, Tavana P, Gyrdymov M, Skobliakov A, Kantsyrev A, et al. Forward-looking insights in laser-generated ultra-intense gamma-ray and neutron sources for nuclear applications and science. *Nat Commun* (2022) 13:170. doi:10.1038/s41467-021-27694-7

6. Habs D, Köster U. Production of medical radioisotopes with high specific activity in photonuclear reactions with g-beams of high intensity and large brilliance. *Appl Phys B* (2011) 103:501–519. doi:10.1007/s00340-010-4278-x

7. Ma Z, Lan H, Wu S, Xu Y, Zhu Z, Luo W. Photonuclear production of medical isotopes 62, 64Cu using intense laser-plasma electron source. *Matter Radiat Extremes* (2019) 4:064401. doi:10.1063/1.5100925

8. Loveman R, Bendahan J, Gozani T, Stevenson J. Time of flight fast neutron radiography. *Nucl Instrum Methods Phys Res B* (1995) 99:765–768. doi:10.1016/0168-583X(94)00684-9

9. Lan Z, Arikawa Y, Mirfayzi SR, Morace A, Hayakawa T, Sato H, et al. Single-shot laser-driven neutron resonance spectroscopy for temperature profiling. *Nat Commun* (2024) 15:5365. doi:10.1038/s42147-024-03210-x

10. Feng J, Li Y, Tan J, Wang W, Li Y, Zhang X, et al. Laser Plasma-Accelerated Ultra-Intense Electron Beam for Efficiently Exciting Nuclear Isomers. *Laser Photonics Rev* (2023) 17:2300514. doi:10.1002/lpor.202300514

11. Negoita F, Roth M, Thirolf PG, Tudisco S, Hannachi F, Moustaizis S, et al. Laser driven nuclear physics at ELI-NP. *Rom Rep Phys* (2016) 68:S37–S144

12. Chen SN, Negoita F, Spohr K, d'Humières E, Pomerantz I, Fuchs J. Extreme brightness laser-based neutron pulses as a pathway for investigating nucleosynthesis in the laboratory. *Matter Radiat Extremes* (2019) 4:054402. doi:10.1063/1.5081666

13. Mirani F, Calzolari D, Formenti A, Passoni M. Superintense laser-driven photon activation analysis. *Commun Phys* (2021) 4:185. doi:10.1038/s42005-021-00685-2

14. Andreev NE, Kirsanov VI, Gorbunov LM. Stimulated processes and self-modulation of a short intense laser pulse in the laser wake-field accelerator. *Phys Plasmas* (1995) 2:2573. doi:10.1063/1.871152

15. Esarey E, Schroeder CB, Leemans WP. Physics of laser-driven plasma-based electron accelerators. *Rev Mod Phys* (2009) 81:1229–1285. doi:10.1103/RevModPhys.81.1229

16. Lemos N, Albert F, Shaw JL, Papp D, Polanek R, King P, et al. Bremsstrahlung hard x-ray source driven by an electron beam from a self-modulated laser wakefield accelerator. *Plasma Phys Control Fusion* (2018) 60:054008. doi:10.1088/1361-6587/aab3b5

17. Lemos N, Albert F, Shaw JL, Papp D, Polanek R, King P, et al. X-ray sources using a picosecond laser driven plasma accelerator. *Phys Plasmas* (2019) 26:083110. doi:10.1063/1.5091798

18. Stoyer MA, Sangster TC, Henry EA, Cable MD, Cowan TE, Hatchett SP, et al. Nuclear diagnostics for petawatt experiments. *Rev Sci Instrum* (2001) 72:767. doi:10.1063/1.1319355

19. Norreys PA, Santala M, Clark EL, Zepf M, Watts I, Tatarakis M, et al. Observation of a highly directional gamma-ray beam from ultra-short, ultra-intense laser pulse interactions with solid targets. *Phys Plasmas* (1999) 6:2150. doi:10.1063/1.873466

20. Courtois C, Edwards R, Compant La Fontaine A, Aedy C, Barbotin M, Bazzoli S, et al. Characterisation of a MeV Bremsstrahlung x-ray source produced from a high intensity laser for high areal density object radiography. *Phys Plasmas* (2013) 20:083114. doi:10.1063/1.4818505

21. Pukhov A, Sheng ZM, Meyer-ter-Vehn J. Particle acceleration in relativistic laser channels. *Phys Plasmas* (1999) 6:2847–2854. doi:10.1063/1.873242

22. Pukhov A. Strong field interaction of laser radiation. *Rep Prog Phys* (2002) 66:47. doi:10.1088/0034-4885/66/1/202

23. Shen X, Pukhov A, Rosmej O, Andreev N. Cross-Filament Stochastic Acceleration of Electrons in Kilojoule Picosecond Laser Interactions with Near-Critical-Density Plasma. *Phys Rev Appl* (2022) 18:064091. doi:10.1103/PhysRevApplied.18.064091

24. Bochkarev SG, Brantov AV, Bychenkov VY, Torshin DV, Kovalev VF, Baidin GV, et al. Stochastic electron acceleration in plasma waves driven by a high-power subpicosecond laser pulse. *Plasma Phys Rep* (2014) 40:202–214. doi:10.1134/S1063780X1403002

25. Bagnoud V, Aurand B, Blazevic A, Borneis S, Bruske C, Ecker B, et al. Commissioning and early experiments of the PHELIX facility. *Appl Phys B* (2010) 100:137–150. doi:10.1007/s00340-009-3855-7

26. Major Z, Eisenbarth U, Zielbauer B, Brabetz C, Ohland JB, Zobus Y, et al. High-energy laser facility PHELIX at GSI: latest advances and extended capabilities. *High Power Laser Sci Eng* (2024) 12. doi:10.1017/hpl.2024.17

27. Borisenko N, Akunets A, Borisenko L, Gromov A, Orekhov A, Pastukhov A, et al. Noizy low-density targets that worked as bright emitters under laser illumination. *J Phys Conf Ser* (2022) 1692:012026. doi:10.1088/1742-6596/1692/1/012026

28. Rosmej ON, Andreev N, Zaehter S, Zahn N, Christ P, Borm B, et al. Interaction of relativistically intense laser pulses with long-scale near critical plasmas for optimization of laser based sources of MeV electrons and gamma-rays. *New J Phys* (2019) 21:043044. doi:10.1088/1367-2630/ab1047

29. Rosmej ON, Gyrdymov M, Günther MM, Andreev NE, Tavana P, Neumayer P, et al. High-current laser-driven beams of relativistic electrons for high energy density research. *Plasma Phys Control Fusion* (2020) 62:115024. doi:10.1088/1361-6587/abb24e

30. Rosmej ON, Gyrdymov M, Andreev NE, et al. Advanced plasma target from pre-ionized low-density foam for effective and robust direct laser acceleration of electrons. *High Power Laser Sci Eng* (2025) 13. doi:10.1017/hpl.2024.85

31. Tavana P, Bukharskii N, Gyrdymov M, Spillmann U, Zahter S, Cikhardt J, et al. Ultra-high efficiency bremsstrahlung production in the interaction of direct laser-accelerated electrons with high-Z material. *Front Phys* (2023) 11:1178967. doi:10.3389/fphy.2023.1178967

32. Cikhardt J, Gyrdymov M, Zähter S, Tavana P, Günther MM, Bukharskii N, et al. Characterization of bright betatron radiation generated by direct laser acceleration of electrons in plasma of near critical density. *Matter Radiat Extremes* (2024) 9:027201. doi:10.1063/5.0181119

33. Gyrdymov M, Cikhardt J, Tavana P, Borisenko NG, Guskov SY, Yakhin RA, et al. High-brightness betatron emission from the interaction of a sub picosecond laser pulse with pre-ionized low-density polymer foam for ICF research. *Sci Rep* (2024) 14:14785. doi:10.1038/s41598-024-65490-7

34. Wilks SC, Kruer WL, Tabak M, Langdon AB. Absorption of Ultra-Intense Laser Pulses. Phys Rev Lett (1992) 69:1383–1386. doi:10.1103/PhysRevLett.69.1383

35. Agostinelli S, Allison J, Amako K, Apostolakis J, Araujo H, Arce P, et al. GEANT4 - a simulation toolkit. *Nucl Instrum Methods Phys Res A* (2003) 506:250–303. doi:10.1016/S0168-9002(03)01368-8 (GEANT4, RRID: SCR_014825)

36. Salvat F. *PENELOPE-2018: A Code System for Monte Carlo Simulation of Electron and Photon Transport*. Paris: OECD Nuclear Energy Agency (2019). (PENELOPE, RRID: SCR_014381)

37. Günther MM, Britz A, Clarke RJ, Harres K, Hoffmeister G, Nürnberg F, et al. Nuclear activation-based imaging spectroscopy. *Rev Sci Instrum* (2013) 84:073305. doi:10.1063/1.4812341

38. Schumaker W, Sarri G, Vargas M, Zhao Z, Behm K, Chvykov V, et al. Measurements of high-energy radiation generation from laser-wakefield accelerated electron beams. *Phys Plasmas* (2014) 21:056704. doi:10.1063/1.4875336

39. Bonnet T, Comet M, Denis-Petit D, Gobet F, Hannachi F, Tarisien M, et al. Response functions of imaging plates to photons, electrons and 4He particles. *Rev Sci Instrum* (2013) 84:103510. doi:10.1063/1.4826084

40. Horst F, Fehrenbacher G, Radon T, Kozlova E, Rosmej O. Measurement of the dose distribution in the vicinity of a high-intensity laser–solid interaction. Nucl Instrum Methods Phys Res A (2015) 786:1–6. doi:10.1016/j.nima.2015.03.011

41. Czarnecki D, et al. Nuclear Instruments and Methods in Physics Research Section A. *Nucl Instrum Methods Phys Res A* (2015) 782:69–76. doi:10.1016/j.nima.2015.02.010

42. Agostinelli S, Allison J, Amako K, Apostolakis J, Araujo H, Arce P, et al. GEANT4 - a simulation toolkit. *Nucl Instrum Methods Phys Res A* (2003) 506:250–303. doi:10.1016/S0168-9002(03)01368-8 (GEANT4, RRID: SCR_014825)

43. Kerr SM, Rusby D, Williams GJ, Meaney K, Schlossberg DJ, Aghedo A, et al. Development of a bright MeV photon source with compound parabolic concentrator targets on the National Ignition Facility Advanced Radiographic Capability (NIF-ARC) laser. *Phys Plasmas* (2023) 30:013101. doi:10.1063/5.0124539

44. Schwoerer H, Beleites B, Magill J, editors. *Lasers and Nuclei: Applications of Ultrahigh Intensity Lasers in Nuclear Science*. Berlin, Heidelberg: Springer (2010). doi:10.1007/978-3-642-02044-5

45. Koning AJ, Rochman D, Sublet JC, Dzysiuk N, Fleming M, van der Marck S. TENDL: Complete Nuclear Data Library for Innovative Nuclear Applications. *Nucl Data Sheets* (2019) 155:1–55. doi:10.1016/j.nds.2019.01.002

703 46. Rising M, Armstrong J, Bolding S, Brown F, Bull J, Burke T, et al. MCNP® code v.6.3.0 release
704 notes. *Los Alamos National Laboratory* (2022). (MCNP, RRID: SCR_014765)